Chapter 5
Whole Cells Imaged by Hard X-ray Transmission Microscopy

Zhiting Liang, Yong Guan, Shan Chen and Yangchao Tian

5.1 Introduction

The resolution of conventional light microscopes is diffraction limited. Super-resolution optical microscopies (Chap. 3) have been developed to reach tens of nanometer resolution but are only able to detect fluorescent labels (Huang 2010). Transmission electron microscopy (TEM) is used to analyze the structure of cells at sub-nanometer resolution (Chap. 8), but based on the low penetrating power of electrons, larger cells must first be sliced into 50–500-nm sections (Barcena and Koster 2009). Cryo focused ion beam (FIB) milling for serial block face imaging in the scanning electron microscope (SEM, Chap. 8) is an efficient method to achieve three-dimensional (3D) data of samples with a lateral pixel size of less than 7.5 nm and slice thickness better than 30 nm in Z (Schertel et al. 2013). With the development of high-brilliance synchrotron radiation light sources and high-precision X-ray-focusing optics, high spatial resolution transmission X-ray microscopy (TXM) is developing rapidly with significantly improved spatial resolution. Soft X-ray transmission microscopy (STXM) with a spatial resolution of about 12 nm has been reported (Chao et al. 2009), and hard X-ray microscopy resolution is down

Y. Tian (✉) · Z. Liang · Y. Guan · S. Chen
National Synchrotron Radiation Laboratory, University of Science and Technology of China, 3#317, No.42, Hezuohua South Road, Hefei, 230029 Anhui, P. R. China
e-mail: ychtian@ustc.edu.cn

Z. Liang
e-mail: zhiting@mail.ustc.edu.cn

Y. Guan
e-mail: yongg@ustc.edu.cn

S. Chen
e-mail: Chen3@mail.ustc.edu.cn

© Springer International Publishing Switzerland 2015

T. E. S. Dahms and K. J. Czymmek (eds.), *Advanced Microscopy in Mycology,*
Fungal Biology, DOI 10.1007/978-3-319-22437-4_5

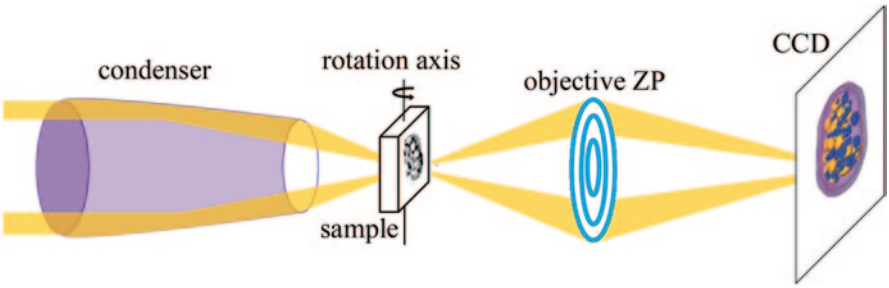

Fig. 5.1 Schematic of the soft X-ray transmission microscopy. Condenser: It focuses a hollow central cone of X-ray onto the sample through the inner surface reflecting. Rotation axis: Sample rotates around the axis to get projections at different angles. Objective zone plate *(ZP)*: It is used as an objective lens for X-ray microscopy. Charged-coupled device *(CCD):* It is a detector

to 30 nm (Chen et al. 2011). TXM has a number of advantages for the examination of biological specimens and material samples. One of the main advantages of this method is the ability to obtain a 3D image of the whole cell (rather than only fluorescently labeled structures), without the need for sectioning required by other methods (i.e., TEM).

TXMs can be divided into soft and hard X-ray microscopes depending on their working photon energy range. A schematic of the soft X-ray microscope is shown in Fig. 5.1. Soft X-ray microscopy was developed, in part, to provide a complementary spatial resolution between optical and electron microscopy and to make full use of the high natural absorption contrast between organic materials and water for photon energies between the K-absorption edge of oxygen ($E \approx 530$ eV or $\lambda = 2.34$ nm) and carbon ($E \approx 280$ eV or $\lambda = 4.43$ nm). The photon energies of the so-called "water window" are especially suitable for imaging samples in aqueous media. The only step required to prepare biological samples for cryo-STXM is plunging the sample into cryogenic liquid nitrogen for vitrification, to protect the sample from radiation damage (X-rays; Weiss et al. 2000) and vacuum inside the microscope chamber (Carzaniga 2013). Correlated cryo-STXM and cryo-fluorescence show that vitrifying the specimen significantly enhances the lifetime of the fluorophore (Le Gros 2009). Usually samples are screened by light microscopy, before transfer to the cryo-STXM sample station, to select appropriate cells, avoid cracks in the ice, debris, and thick ice (Duke 2013). Thus, hydrated biological specimens can be imaged in the photon energy range of the water window with no chemical fixation, dehydration, chemical staining, or physical sectioning. Cryo-STXM is used to visualize the internal architecture of fully hydrated cells (Scherfeld et al. 1998; Chichon et al. 2012; Muller et al. 2012; Hagen et al. 2012; Carrascosa et al. 2009; Drescher et al. 2013; Carzaniga et al. 2013; Hummel et al. 2012), including intact eukaryotic cells (Larabell and Le Gros 2004; Le Gros 2005; Parkinson et al. 2008; Parkinson et al. 2012; Uchida et al. 2009; McDermott et al. 2012) at high spatial resolution (50 nm or better). Recently, higher resolution STXMs have been developed and applied to reveal subcellular structures in whole cells (Schneider et al. 2010).

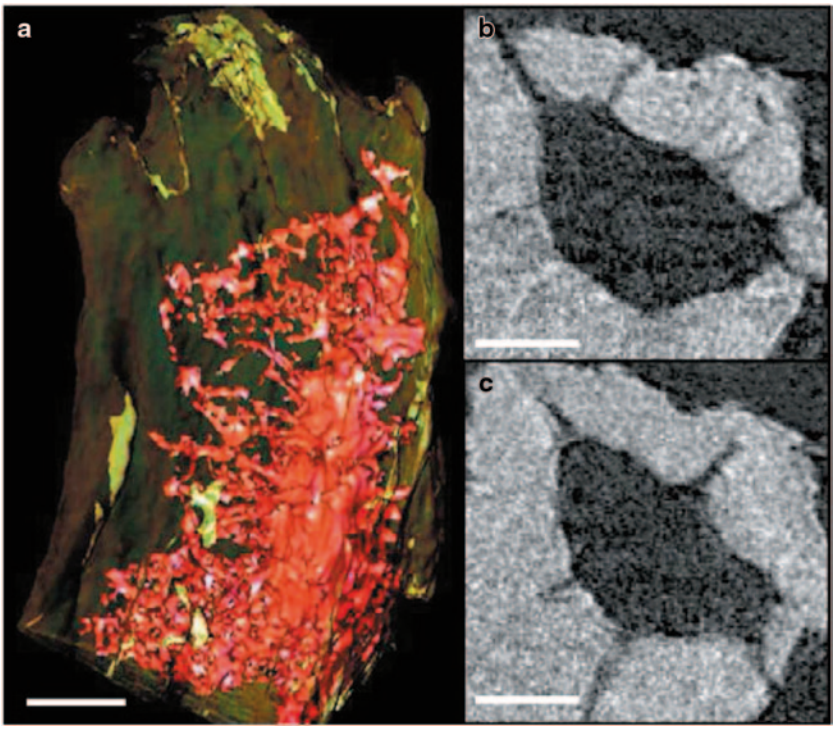

Fig. 5.2 **a** Three-dimensional reconstruction of a single lacuna surrounded by canalicular network (colored red) form mouse tibia trabecula (colored translucent yellow). **b**, **c** Reconstructed slices show processes extending from the lacuna. Scale bar is 5 μm in panel **a** and 2 μm in panels **b** and **c**. (Source: Andrews et al. 2010)

However, because of the low-penetration power of soft X-rays and the small depth of focus (DOF) of soft X-ray microscopy, biological sample size is limited, especially when 3D tomographic imaging is required. Thus, soft X-ray microscopy is not suitable for imaging large biological samples, including eukaryotic cells. Hard X-ray microscopy can overcome this limitation since it has high penetration and large DOF to facilitate 3D tomography of thicker samples with excellent resolution (Andrews et al. 2010). Hard X-ray transmission microscopy has been employed to observe various biological specimens (Yang et al. 2010; Zheng et al. 2012; Jeon et al. 2008; Zhang et al. 2013). Andrews et al. used hard X-ray transmission microscopy to image the internal structures and networks of mouse cancellous bone with high resolution (~30–40 nm; Andrews et al. 2010). Reconstructed data revealed the canalicular network including processes extending from the lacuna. Moreover, the 3D microstructure of a single lacuna found within a trabecula showed its shape, geometry, and surrounding canalicular network (Fig. 5.2a). The reconstructed slices (Fig. 5.2b, c) further show fine cell processes extending from lacunae in high-resolution detail (Andrews et al. 2010). In order to understand the internalization of

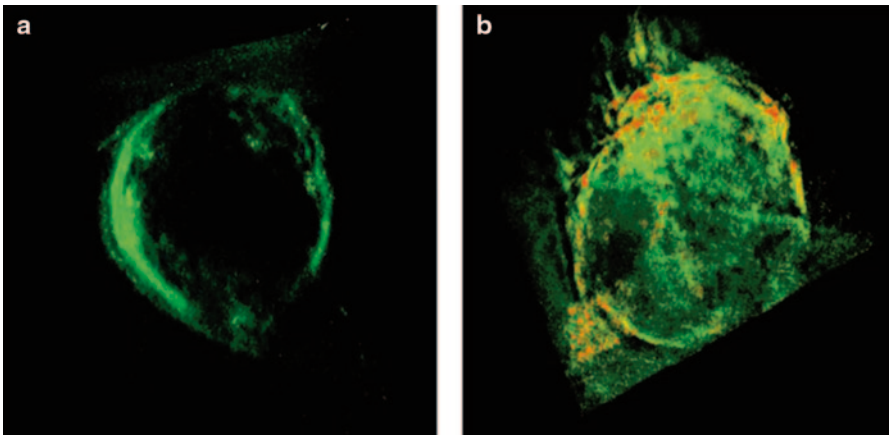

Fig. 5.3 Three-dimensional reconstructions of **a** a normal HeLa cell and **b** a cell after incubation with TiO_2 nanoparticles for 6 h (*red color* indicates the nanoparticle aggregates in the cell membrane). (Source: Zhang et al. 2013)

nanoparticles in cells, Cai et al. employed high-resolution hard X-ray transmission microscopy to investigate the cellular uptake and distribution of TiO_2 nanoparticles using HeLa cells. By rotating on the sample stage from −75 to +75° in 1° intervals, 151 projection images of a HeLa cell were collected. The 3D-reconstructed tomography maps of cells treated with TiO_2 nanoparticles showed that their aggregates were mainly distributed over the cell membrane surface (Fig. 5.3), which was confirmed by TEM. The results demonstrate that hard X-ray transmission microscopy has the ability to image the cellular distribution of nanoparticle aggregates and can be applied as a complementary analytical method to image the 3D distribution of nanoparticle aggregates in cells (Zhang et al. 2013).

Currently, hard X-ray tomography applied to biological imaging is in its initial stages, but results obtained to date demonstrate that it can provide a complementary tool for cellular imaging and analysis. In this chapter, we provide an overview of 3D microstructural analysis of yeast using hard X-ray transmission microscopy. Biological materials such as yeast have complex subcellular and intercellular structures, so their whole cell imaging requires a 3D technique on the nanometer scale with sufficient sample penetration. Hard X-ray microscopy meets these requirements by providing much better spatial resolution of cellular structures than light microscopy and by viewing internal structures of a whole cell without the need of sectioning. Moreover, when combined with tomographic procedures, hard X-ray microscopy can be used to make a complete 3D reconstruction of a whole cell to provide subcellular and intercellular microstructural information not available to conventional imaging techniques. Although the spatial resolution of hard X-ray microscopy is slightly less than that of soft X-ray microscopy, it can image large eukaryotic cells with thickness up to several tens of micrometers.

5.2 High-Resolution X-ray Microscopy

Since the refractive index of X-rays is close to unity for most materials, refractive lenses, similar to those used in light microscopy, are not applicable due to the strong absorption of X-rays by most materials. An ellipsoidal capillary has been developed as a condenser to focus X-rays, and a Fresnel zone plate is used as an objective lens. Figure 5.4 shows the layout of the transmission hard X-ray microscopy at the beamline U7A housed at the National Synchrotron Radiation Lab (NSRL) of China.

5.2.1 Light Source

When carrying out X-ray tomography, sample drift and noise caused by unavoidable instabilities in the microscope system will degrade the quality and clarity of the projected images and therefore the quality of final 3D tomographic reconstructions. Thus, it is important to collect the entire set of tomographic data with high signal-to-noise ratio in the shortest period of time, requiring a highly stable X-ray source such as that found at a synchrotron lab. When charged particles are accelerated in a radial fashion with bending magnets at the corners and insertion devices, wigglers, or undulators used in the straight sections of the storage ring (see Fig. 5.4), synchrotron radiation is produced. This radiation has a broad spectrum, which covers the infrared to hard X-ray regions and a high flux, which can allow rapid experiments. Thus, a synchrotron light source is the optimal source for high-resolution X-ray imaging. High-resolution X-ray microscopy facilities based on synchrotron radiation have been developed worldwide in the past decade. There are more than 47

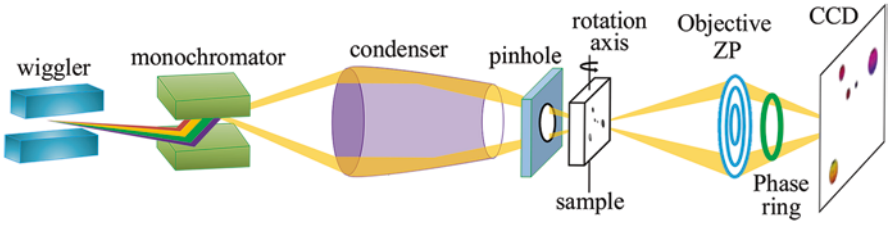

Fig. 5.4 The layout of the transmission X-ray microscopy *(TXM)* at the beamline U7A of the National Synchrotron Radiation Lab of China. Wiggler: It is composed of a series of magnets that are designed to periodically laterally deflect charged particles inside the storage ring of the synchrotron. These deflections create a change in acceleration, thus producing radiation with sufficient brightness and flux in the energy range of hard X-ray. Monochromator: It is an optical device that transmits a narrow band of wavelengths of light chosen from a wider range of wavelengths from the input. Pinhole: It is used as a monochromator to choose the wavelength range that can be transmitted. Phase ring: It causes a phase shift of the X-ray beam not diffracted by the sample, of either $\pi/2$ or $3\pi/2$. The phase contrast image is formed by the interference of the phase-shifted undiffracted light with the unshifted light diffracted by the sample light, translating phase modulations of the sample into intensity modulations in the image plane

synchrotron light sources worldwide (see http://lightsources.org/regions for their names, locations, and homepage). Most of the experimental end stations are open for applications from international users. Users can source appropriate equipment and their parameters from the homepage of each synchrotron, and then contact the person in charge of the end station to discuss related issues. The time available for doing an experiment depends on the operating conditions and the experimental arrangement at that moment. The NSRL storage ring operates with an electron beam energy of 0.8 GeV and a maximum current of 250 mA. A 6-T superconducting wiggler was installed at NSRL to produce hard X-rays with sufficient brightness and flux: 3.5×10^9 photons/s at a beam size of 12×13 mm^2 in the energy range of 7–12 keV. An existing beamline (U7A at NSRL), having a simple optical system designed to provide maximum output at a given energy resolution with acceptable cost, was selected to install the transmission X-ray microscope.

5.2.2 Focusing Optics

Ellipsoidal capillaries have been widely used as focusing optics for both soft and hard X-ray microscopy (Zeng et al. 2008; Guttmann et al. 2009). The ellipsoidal capillary condenser focuses a hollow central cone of illumination onto the sample and the objective zone plate. The source and focus are located at the two focal points of the ellipse generated when imaging the X-ray source with an ellipsoidal reflector. The desired parameters of the reflecting inner surface of the ellipsoidal capillary condenser are determined by two factors: the desired range of illumination angles on the output side and the distance between the X-ray source and the sample position (Zeng et al. 2008). The former should be designed to match the numerical aperture (NA) of the high-resolution objective zone plate. Glass capillaries with smooth inner surfaces can be drawn with a variety of fixed inner and outer diameters. The focusing efficiency of the capillary condenser is over 80% due to lower surface roughness, while the efficiency of the zone plate is only near 10% (Guttmann et al. 2009). An ellipsoidal capillary was installed at the NSRL, and the focusing efficiency measured was 85% (Jinping et al. 2008).

5.2.3 X-ray Microscope Objective Lens

A Fresnel zone plate (Fig. 5.5), used as the objective lens in transmission X-ray microscopy, consists of a circular grating having a period that decreases radially in such a way that the diffraction orders from each zone add up coherently. The latter condition is achieved when all of the diffracted rays are in phase, that is, the optical path difference is $\pi/2$ between adjacent zones, opaque and transparent. The spatial resolution of an X-ray microscope depends on the numerical aperture (NA) of the objective zone plate given by:

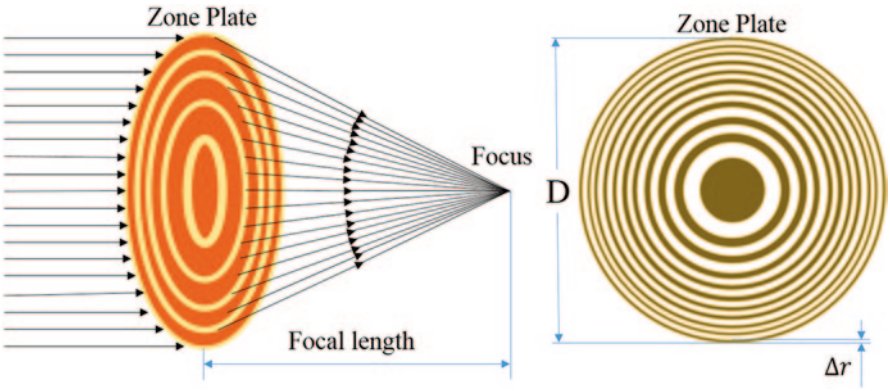

Fig. 5.5 Schematic drawing of a zone plate *(ZP)*. The diameter of the ZP is D and the width of the outermost zone is Δr. ZP is an objective lens for X-ray microscopy and Δr is the most crucial parameter of the system resolution

$$\delta = \frac{0.61}{NA} \times \frac{\lambda}{m} = \frac{1.22\Delta r}{m}, \tag{5.1}$$

where·λ is the incident wavelength, m is the diffracted order, and Δr is the outermost zone width of the zone plate. According to the Rayleigh criterion, δ is the shortest distance between two features that can be resolved in the zone-plate image. The theoretical resolution of an X-ray microscope is proportional to the outermost zone width. The transmission X-ray microscope at NSRL has an objective zone plate lens with an 80 μm diameter and a 45-nm outer zone width, offering 55 nm resolution in the first-order diffraction for a photon energy of 8 keV (Hard X-rays wavelength, λ, of 0.15 nm). Nowadays, zone-doubled Fresnel zone plates with 20-nm outermost zone width are being designed and modeled to achieve a spatial resolution better than 20 nm at the Advance Photon Source at Argonne National Laboratory (Vila-Comamala et al. 2012).

Another objective zone plate parameter that needs to be considered is the DOF, defined by the distance over which the focus intensity is > 80 % of its maximum. The DOF is given by the following equation (Born and Wolf 1999):

$$\mathrm{DOF} = \pm\lambda/\mathrm{NA}^2 = \pm 2\Delta r^2/\lambda, \tag{5.2}$$

where NA is the numerical aperture of the zone plate; λ is the wavelength of the incident X-ray; and Δr is the outermost zone width of the objective zone plate. As demonstrated by this equation, when trying to achieve higher resolution, the DOF decreases. The transmission X-ray microscope at NSRL has a DOF of approximately 52 μm, enabling imaging of relatively thick samples.

5.2.4 The Zernike Phase Ring

The complex refractive index of the object can be expressed as $n = 1 - \delta + i\beta$, where δ is the phase shift term and β is the attenuation term. The δ term describes the diffraction limit, refraction, and the phase shift of the X-rays. For soft biological materials made up primarily of low-Z elements, δ is orders of magnitude (10^3) higher than β for soft materials in the hard X-ray region ($\lambda \approx 1-0.1$ Å; Momose 2005). In other words, in the hard X-ray region, X-ray absorption may produce poor contrast images of soft materials. Thus, X-ray phase contrast has been widely used to study soft biological tissues (Momose et al. 1996; Williams et al. 2008; Pfeiffer et al. 2007). Here, we use X-ray phase contrast imaging prior to absorption imaging of biological samples, which are weakly absorbing. In our recent imaging experiments, Zernike phase contrast was explored to visualize the 3D microstructure of yeasts (Yang et al. 2010; Zheng et al. 2012).

A phase ring (PR; see Figs. 5.4 and 5.6) is located at the back focal plane of the objective zone plate, causing a phase shift of the X-ray beam not diffracted by the sample, of either $\pi/2$ (positive phase contrast) or $3\pi/2$ (negative phase contrast). Positive phase contrast signifies greater optical thickness of the object, corresponding to a brighter image, while negative phase contrast has the opposite relationship (Kagoshima et al. 2001). The phase contrast image is formed by the interference of the phase-shifted undiffracted light with the unshifted light diffracted by the sample, translating phase modulations of the sample into intensity modulations in the image plane (see Fig. 5.6). At NSRL, the PR is made of Au with 2.4 μm thickness and 4 μm width (Tian et al. 2008), able to provide negative Zernike phase contrast. Figure 5.7 illustrates how the phase contrast image is improved over the absorption image, each taken at the same exposure time (Yang et al. 2010).

5.3 Tomographic Data Preprocessing and Reconstruction

5.3.1 Introduction to Tomography

There are many discretely and regularly distributed subcellular structures within a cell, for which their distribution and morphology relate to function. However, projection X-ray microscopy images of cells are two-dimensional (2D) in which many structural features are superimposed, making it difficult to observe and analyze cellular substructures. Therefore, acquiring high-resolution 3D images is desirable. When a series of projections are collected at angular intervals around a rotation axis, it is possible to reconstruct a 3D image of the sample using tomography.

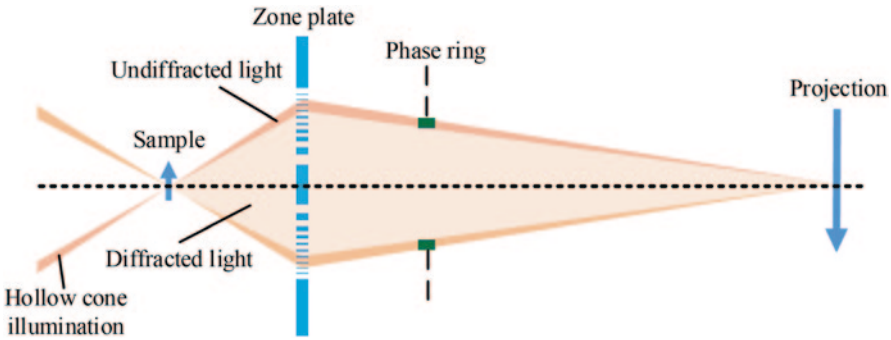

Fig. 5.6 Schematic of the annular phase ring. The phase ring is positioned following the ZP to intercept the undiffracted X-ray light. The thickness is designed to shift the phase of the undiffracted light by $3\pi/2$. The phase contrast image is formed by the interference of the phase-shifted undiffracted light with the unshifted light diffracted by the sample light, translating phase modulations of the sample into intensity modulations in the image plane

5.3.2 Tomographic Data Collection and Processing

For hard X-ray imaging, the projections are collected at 8 keV using the Zernike phase contrast model. When collecting projection images for tomographic reconstruction, the sample holder should permit the sample to remain within the field of view for isotropic data collection over 180° of rotation. However, a flat sample holder usually used for hard X-ray transmission microscopy can only be rotated ±74° before it occludes the X-rays, offering only 75 (or 150) projection images ranging from −74 to 74° in 2° (or 1°) intervals. The 3D internal microstructure of cells can completely be reconstructed based on these projections. While some image artifacts may arise from incomplete data collection, advanced reconstruction methods have been developed to attempt to eliminate such artifacts (Liang et al. 2013; Wang and Jiang 2004; Sidky et al. 2006).

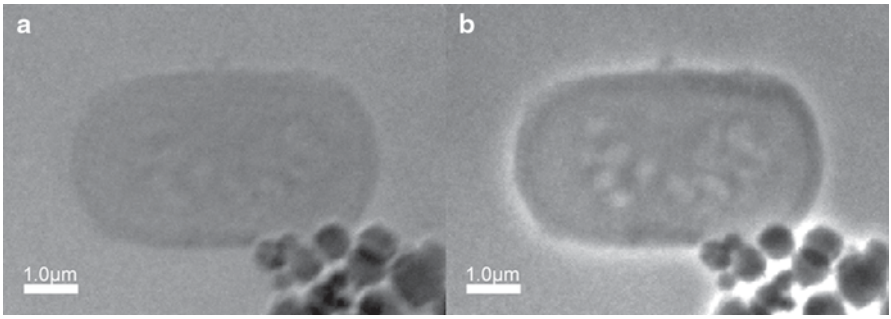

Fig. 5.7 Two models of yeast projections (Yang et al. 2010). **a** Absorption contrast projection of a yeast cell and **b** Zernike phase contrast projection of the same cell

Prior to reconstruction, the raw projections must first be processed. To correct for heterogeneities in sample illumination, which is due to the inhomogeneities of the light source, projections are normalized using a flat-field image collected with no sample in the field of view. Image intensity is normalized by dividing the projection image by the flat-field image, pixel by pixel. It is also necessary to correct for artifacts caused by "bad" pixels on the charged-coupled device (CCD), meaning those that have lost signal strength over the lifetime of the CCD. For each projection and flat-field image, the value of the bad pixel is replaced with a value interpolated from surrounding pixels. The instability of the rotation stage is accounted for by aligning all images to a common rotation axis prior to reconstruction. There are two main approaches: automated alignment (Parkinson et al. 2012) and manual alignment of the fiducial markers (i.e., 100-nm gold particles on the sample holder). Manual alignment is more accurate than automated, so the former is used to acquire initial results quickly, and higher-quality reconstructions can be achieved using the manual approach.

5.3.3 3D Reconstruction

Tomographic reconstruction is pursued once the images are properly processed. 3D sample images can be achieved by combining 2D projections. Numerous reconstruction algorithms have been proposed (Gordon et al. 1970; Andersen and Kak 1984; Raparia et al. 1998; Wang and Jiang 2004; Sidky et al. 2006; Andersen 1989; Zeng 2010), all with associated advantages and disadvantages. Generally speaking, reconstruction algorithms can be divided into two classes. The first class relies on Fourier methods and the central slice theorem (Zeng 2010), often the most popular choice based on the limited computational burden. The other class uses iterative reconstruction methods (Mueller et al. 1999; Liang et al. 2013; Cierniak 2011), which allow prior knowledge to be included in processing, and many regularizations (e.g., total variation minimization; Tian et al. 2011; Sidky and Pan 2008) and filters that can improve the quality of the results. Nevertheless, iterative reconstruction methods consume a large amount of computational time, preventing their widespread use. However, methods using graphics processing units (GPU) to speed up computation would enable these methods to regain more attention (Keck et al. 2009; Pan et al. 2009; Nett et al. 2010).

5.4 Cell Culture and Preparation

The fission yeasts are a particularly good eukaryotic cell model used for many years, particularly for studying the cell cycle and how the shape, size, and distribution of organelles change with environmental conditions (Zheng et al. 2012). The wild-type fission yeast, *Schizosaccharomyces pombe*, was cultured in liquid yeast

extract peptone dextrose (YPD) medium at 25 °C for 12 h, rinsed in 0.2 M PIPES buffer (3×; piperazine-N, N'-bis[2-ethane sulfonic acid]) and fixed with 2% osmium tetroxide (in PIPES; 1 h, 25 °C), rinsed (2×) with PIPES buffer, stained with Reynolds' lead citrate (20 min), dehydrated in a graded ethanol series of 50–100% concentration (EtOH/(water + EtOH)), and then stained by 2% uranyl acetate in 95% ethanol solution (10 min). At last, the cells were spotted on a silicon nitride membrane of 100 nm thickness and air-dried. In this proof of principle, we chose the simplest drying method to show that hard X-ray tomography could be used to image cells. However, it is important to note that air-drying is not the best choice for cell sample preparation, causing drying artifacts, even when the sample had been fixed and ethanol substituted. In future, critical point drying (Lampert 1971), resin-embedded samples, and other new electron microscopy (EM) sample preparation technologies such as high-pressure freezing (McDonald 2007) and self-pressurized rapid freezing (Leunissen and Yi 2009), proven to maintain good sample shape, can be applied to hard X-ray microscopy.

5.5 Cell Organelles Identified

Projections were obtained using the phase contrast model and the photon energy of 8 keV. The 3D structure of the cell was reconstructed using a standard filtered back-projection algorithm (Kak et al. 1988) through a series of projections (Fig. 5.8a; Yang et al. 2010). Slice thickness is related to the pixel size of the CCD, approximately 58.3 nm for our system. The reconstructed cross-slices of cells from two different orientations are shown in Fig. 5.8b, c. The cell wall, with its three-layered structure, is clearly observed in the cross-slices (Fig. 5.8b, c, arrowheads), having a thickness of approximately 400 nm, which is typical for wild-type *S. pombe*. There are numerous small, near-spherical organelles having lower X-ray contrast than surrounding cytoplasm, and other organelles with irregular shape and higher X-ray contrast than the cytoplasm (Fig. 5.8b, c).

Segmentation can provide a way to isolate a specific cellular component from the data set, allowing 3D visualization of that component either alone or with other components. At present, identification of organelles by hard X-ray tomography is complex and difficult. Following heavy metal staining, every organelle of the cell will have a different X-ray absorption compared to the cytoplasm, allowing organelle boundaries to be identified. The density of lipid bodies and mitochondria is greater than the cytoplasm, so those components are more easily stained by heavy metal. Organelles having lower contrast (Fig. 5.8b, c) are consistent with vacuoles that also have low electron density in TEM studies (Konomi et al. 2003; Sajiki et al. 2009) that used comparable staining. Their morphology and distribution is also consistent with vacuoles identified by TEM and fluorescence microscopy (Bone et al. 1998; Mulvihill et al. 2001; Konomi et al. 2003; Takagi et al. 2003). The lower X-ray contrast organelles colored blue with near-spherical shape are identified as vacuoles, and the higher X-ray contrast organelles colored yellow are assigned as

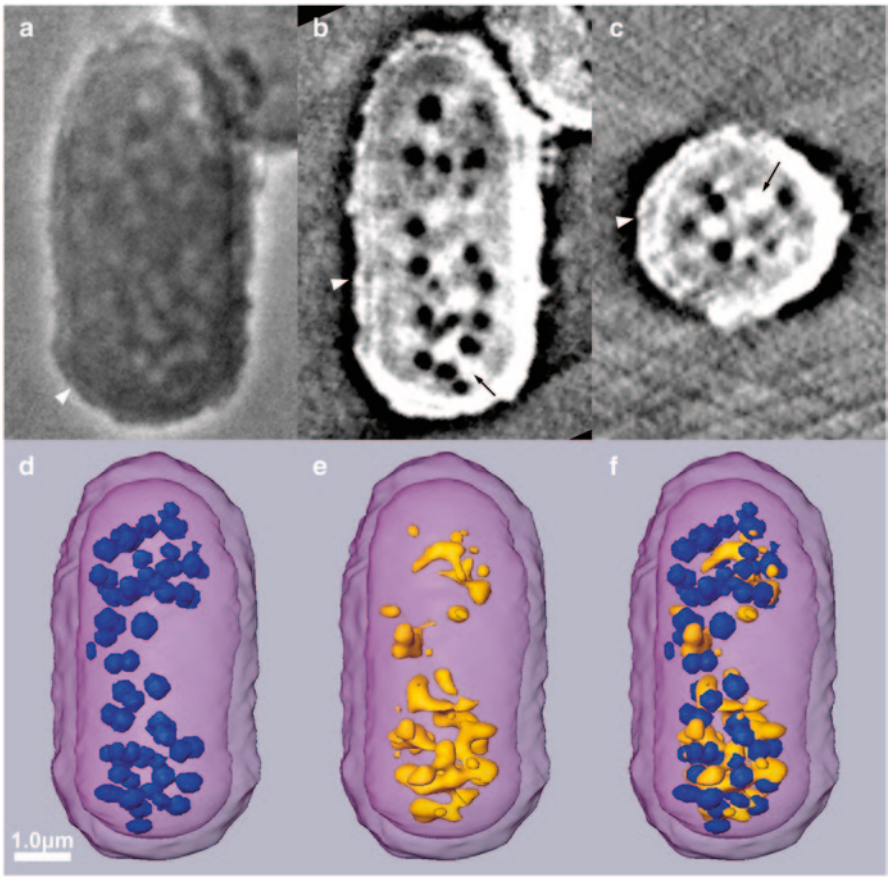

Fig. 5.8 Hard X-ray tomography of a fission yeast cell, *Schizosaccharomyces pombe* (Yang et al. 2010). **a** Projection of the yeast cell. **b**, **c** Reconstructing cross-slices through the cell from vertical orientations. *Arrows* point to the organelles that have higher X-ray contrast than surrounding cytoplasm, and *arrowheads* indicate the three-layer structure of the cell wall. **d**, **e** Organelles are divided into two groups based on their absorption contrast. The lower contrast organelles colored *blue* are identified as vacuoles, and the higher X-ray contrast organelles colored *yellow* are lipid bodies and mitochondria. **f** Total organization and distribution of organelles within a yeast cell

lipid bodies and mitochondria (Fig. 5.8). It is difficult to distinguish mitochondria and lipid bodies based on the hard X-ray tomographic data since resolution is limited, precluding exact organelle classification. By improving the resolution of hard X-ray microscopy in future, organelle identification will be more facile. In future work, the data could be correlated with TEM from the same sample to confirm the identity of mitochondria and lipid bodies based on their shape and size.

5.6 Quantitative Analysis of Organelles in the Cell

Cell size is a critical parameter in initiating cell division, and the number, morphology, and volume of the organelles have a profound influence on the function and viability of a cell (Uchida et al. 2011). Consequently, the quantitative analysis of cellular internal architecture is of great significance in cell science. Since hard X-ray tomography is capable of obtaining 3D architectures of biological samples, it has been used to investigate the yeast cycle at various stages. From the stationary to the growth phase, the shape of yeast transitioned from short and spherical (Fig. 5.9a) to long, thin, and elliptical (Fig. 5.9f). During cell division, a membrane (colored red) formed, and presumably septum cell wall components were also present, but their detection was beyond the resolution limit. The two cells had not yet separated completely (see Fig. 5.9m).

Yeast size is a decisive parameter for cell division, having to reach a minimum size before they begin to divide (Goranov et al. 2009; Jorgensen et al. 2002). During the cell cycle, organelle size must be precisely detected and controlled, both for proper cellular function and correct organelle partitioning (Neumann and Nurse 2007; Rafelski and Marshall 2008; Fagarasanu et al. 2007). Thus, in relation to cell growth and division, cell size, major organelle volume, and organelle to cell volume ratio were quantified (Table 5.1). As expected, cell volume gradually increases from the stationary phase (54.3 μm^3) to division (81.4 μm^3). The ratio of total major organelle to cell volume (O:C ratio) in each phase was 23.8, 10.6, and 11.1% (Fig. 5.10), for stationary, growth, and division phases, respectively. A similar ratio was calculated for vacuoles, lipid bodies, and mitochondria alone (Fig. 5.10). From the growth to division phase, the O:C ratio for lipid bodies and mitochondria remained approximately stable (5.7–5.9%) as did that for vacuoles (4.9–5.2%). That is to say that the ratios existing between cell size and organelle volumes are consistent during the division and growth phases. On the contrary, the O:C ratio for all organelles, vacuoles, lipid bodies, and mitochondria in the stationary phase are higher than those during growth and division phases, indicating an increase in organelle volume during the stationary phase. Further, organelle shape varies in all three phases, with characteristic shapes in each phase. It can be concluded that hard X-ray microscopy is suitable for cellular imaging when some contrast enhancement method is introduced, such as Zernike phase contrast and heavy metal staining. Since samples were air-dried, shrinkage differences in the stationary and growth phases would influence the volume and ratios of the cells. Nonetheless, we demonstrated the ability of hard X-ray tomography to quantify and image cells. In future work, more sophisticated drying technologies developed for electron microscopy can be introduced to hard X-ray microscopy. The unique ability of hard X-ray microscopy to acquire images of whole, large cells in 3D could make it a complementary tool for imaging cells and providing useful information in cell biology (Yang et al. 2010).

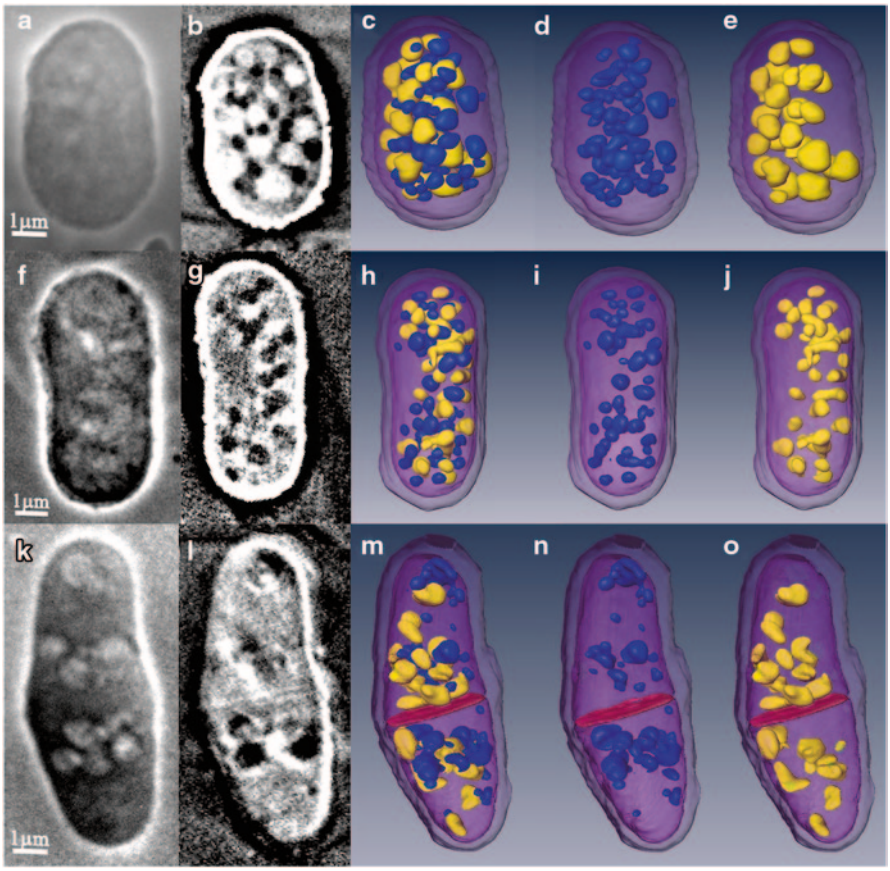

Fig. 5.9 Different phases of a fission yeast cell, *Schizosaccharomyces pombe,* imaged by hard X-ray tomography (Zheng et al. 2012). The three rows of images correspond to a cell in the stationary phase, a single adult cell, and a dividing yeast cell. The first column is the two-dimensional (2D) projection image, the second to fifth columns are reconstruction slices, the whole cells, vacuoles, and lipid bodies and mitochondria, respectively. (*m*, *n,* and *o*) A dense band between the mother and daughter cells is colored *red*. The organelles colored *blue* with near-spherical shape are identified as vacuoles, and the organelles colored *yellow* are assigned as lipid bodies and mitochondria

5.7 Future Developments of Hard X-ray Microscopy

In this chapter, we demonstrate that hard X-ray microscopy, using high penetration power and a large DOF, is a powerful tool for studying high-resolution 3D cell architecture. Contrast enhancement can be achieved with Zernike phase contrast and heavy metal staining. Based on the tomographic data, we can observe microstructural changes of yeasts during the cell cycle. While we demonstrate that hard X-ray microscopy and tomography have the ability to examine internal cellular ultrastructures, there is still room to improve spatial resolution. With the develop-

Table 5.1 Dimensions and volumes of organelles and cells from Fig. 5.9. (Source: Zheng et al. 2012)

Feature	Cell		
	Stationary	Growth	Division
Cell length (μm)	6.1	7.2	9.7
Cell width (μm)	4.1	3.5	5.1
Cell volume (μm^3)	54.3	68.2	81.4
Vol. organelles (μm^3)	12.9	7.2	10.0
Vol. lipid bodies and mitochondria (μm^3)	7.3	3.9	4.8
Vol. vacuoles (μm^3)	5.57	3.3	4.2

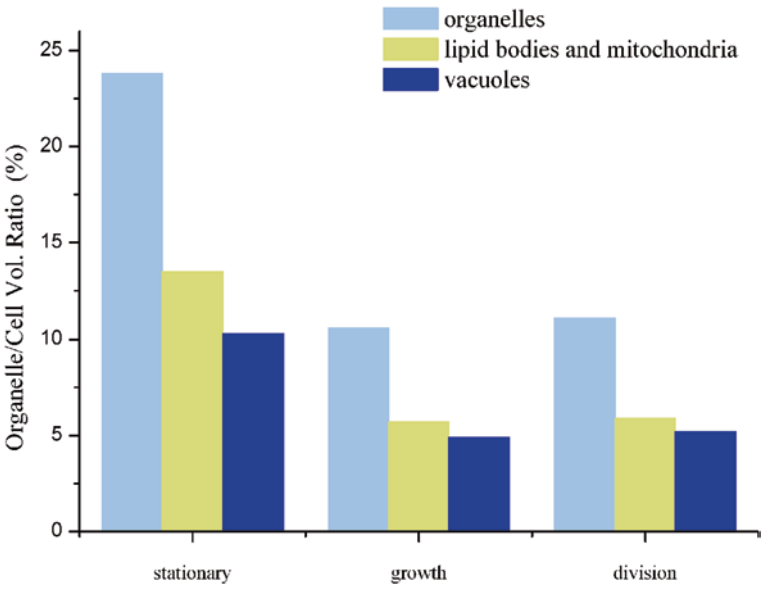

Fig. 5.10 The organelle to cell volume ratio, including major organelles, vacuoles, lipid bodies, and mitochondria, during **a** stationary phase, **b** cell growth, and **c** division phases of the cell cycle. (Source: Zheng et al. 2012)

ment of micro- and nanofabrication technology, the width of the outer zone of zone plates will be smaller, and the focusing diffraction efficiencies will be improved. In addition, the stability of the rotating station and data-processing software will also be promoted. Therefore, higher resolution will be achieved. Cryo-fixation, able to combat the radiation damage from X-rays and maintain the sample morphology, can be easily introduced into sample preparation methods for hard X-ray imaging. Furthermore, hard X-ray microscopy/tomography can be used in a correlative manner with other techniques to identify organelles. The data obtained by hard X-ray tomography can be correlated with electron microscopy of the same sample to identify

organelles by morphology and position. Fluorescence imaging is another mature technology (Smith et al. 2013) that can be combined with hard X-ray microscopy to determine the position of fluorescently tagged molecules in the reconstruction images. Such integrative and correlative techniques will extend the potential of hard X-ray microscopy in cell imaging.

References

Andersen AH (1989) Algebraic reconstruction in CT from limited views. IEEE Trans Med Imaging 8(1):50–55. doi:10.1109/42.20361

Andersen A, Kak A (1984) Simultaneous algebraic reconstruction technique (SART): a superior implementation of the ART algorithm. Ultrason Imaging 6(1):81–94

Andrews JC, Almeida E, van der Meulen MC, Alwood JS, Lee C, Liu Y, Chen J, Meirer F, Feser M, Gelb J, Rudati J, Tkachuk A, Yun W, Pianetta P (2010) Nanoscale X-ray microscopic imaging of mammalian mineralized tissue. Microsc Microanal 16(3):327–336. doi:10.1017/S1431927610000231

Barcena M, Koster AJ (2009) Electron tomography in life science. Semin Cell Dev Biol 20 (8):920–930. doi:10.1016/j.semcdb.2009.07.008

Bone N, Millar JBA, Toda T, Armstrong J (1998) Regulated vacuole fusion and fission in *Schizosaccharomyces pombe*: an osmotic response dependent on MAP kinases. Curr Biol 8(3):135–144. doi:10.1016/S0960-9822(98)00060-8

Born M, Wolf E (1999) Principles of optics: electromagnetic theory of propagation, interference and diffraction of light. CUP Archive, New York

Carrascosa JL, Chichon FJ, Pereiro E, Rodriguez MJ, Fernandez JJ, Esteban M, Heim S, Guttmann P, Schneider G (2009) Cryo-X-ray tomography of vaccinia virus membranes and inner compartments. J Struct Biol 168(2):234–239. doi:10.1016/j.jsb.2009.07.009

Carzaniga R, Domart MC, Collinson LM, Duke E (2013) Cryo-soft X-ray tomography: a journey into the world of the native-state cell. Protoplasma. doi:10.1007/s00709-013-0583-y

Chao W, Kim J, Rekawa S, Fischer P, Anderson EH (2009) Demonstration of 12 nm resolution fresnel zone plate lens based soft X-ray microscopy. Opt Express 17(20):17669–17677

Chen YT, Chen TY, Yi JM, Chu YS, Lee WK, Wang CL, Kempson IM, Hwu Y, Gajdosik V, Margaritondo G (2011) Hard x-ray zernike microscopy reaches 30 nm resolution. Opt Lett 36(7):1269–1271

Chichon FJ, Rodriguez MJ, Pereiro E, Chiappi M, Perdiguero B, Guttmann P, Werner S, Rehbein S, Schneider G, Esteban M, Carrascosa JL (2012) Cryo X-ray nano-tomography of vaccinia virus infected cells. J Struct Biol 177(2):202–211. doi:10.1016/j.jsb.2011.12.001

Cierniak R (2011) Algebraic reconstruction techniques. In: X-ray computed tomography in biomedical engineering. Springer, London, pp 233–265

Drescher D, Guttmann P, Buchner T, Werner S, Laube G, Hornemann A, Tarek B, Schneider G, Kneipp J (2013) Specific biomolecule corona is associated with ring-shaped organization of silver nanoparticles in cells. Nanoscale 5(19):9193–9198. doi:10.1039/c3nr02129g

Duke EM, Razi M, Weston A, Guttmann P, Werner S, Henzler K, Schneider G, Tooze SA, Collinson LM (2013) Imaging endosomes and autophagosomes in whole mammalian cells using correlative cryo-fluorescence and cryo-soft X-ray microscopy (cryo-CLXM). Ultramicroscopy 143:77–87

Fagarasanu A, Fagarasanu M, Rachubinski RA (2007) Maintaining peroxisome populations: a story of division and inheritance. Annu Rev Cell Dev Biol 23:321–344. doi:10.1146/annurev.cellbio.23.090506.123456

Goranov AI, Cook M, Ricicova M, Ben-Ari G, Gonzalez C, Hansen C, Tyers M, Amon A (2009) The rate of cell growth is governed by cell cycle stage. Genes Dev 23(12):1408–1422. doi:10.1101/gad.1777309

Gordon R, Bender R, Herman GT (1970) Algebraic reconstruction techniques (ART) for three-dimensional electron microscopy and X-ray photography. J Theor Biol 29(3):471–481

Guttmann P, Zeng X, Feser M, Heim S, Yun W, Schneider G (2009) Ellipsoidal capillary as condenser for the BESSY full-field x-ray microscope. 9th international conference on X-Ray microscopy 186. doi:Artn 012064Doi 10.1088/1742-6596/186/1/012064

Hagen C, Guttmann P, Klupp B, Werner S, Rehbein S, Mettenleiter TC, Schneider G, Grunewald K (2012) Correlative VIS-fluorescence and soft X-ray cryo-microscopy/tomography of adherent cells. J Struct Biol 177(2):193–201. doi:10.1016/j.jsb.2011.12.012

Huang B (2010) Super-resolution optical microscopy: multiple choices. Curr Opin Chem Biol 14(1):10–14. doi:10.1016/j.cbpa.2009.10.013

Hummel E, Guttmann P, Werner S, Tarek B, Schneider G, Kunz M, Frangakis AS, Westermann B (2012) 3D ultrastructural organization of whole chlamydomonas reinhardtii cells studied by nanoscale soft X-ray tomography. PLoS ONE 7(12): e53293. doi:ARTN e53293DOI 10.1371/journal.pone.0053293

Jeon SY, Goo JW, Hong SP, Oh TH, Youn HS, Lee WS (2008) A new method for investigation of the hair shaft: hard X-ray microscopy with a 90-nm spatial resolution. Yonsei Med J 49(2):337–340. doi:10.3349/ymj.2008.49.2.337

Jinping T, Wenjie L, Jie C, Gang L, Ying X, Longhua L, Xinlong H, Yangchao T (2008) The design and test of ellipsoidal glass capillaries as condensers for X-ray microscope. Nucl Tech 31(09):671–675

Jorgensen P, Nishikawa JL, Breitkreutz BJ, Tyers M (2002) Systematic identification of pathways that couple cell growth and division in yeast. Science 297(5580):395–400. doi:10.1126/science.1070850

Kagoshima Y, Ibuki T, Yokoyama Y, Tsusaka Y, Matsui J, Takai K, Aino M (2001) 10 keV X-ray phase-contrast microscopy for observing transparent specimens. Jpn J Appl Phys 2 40 (11A):L1190–L1192. doi:10.1143/Jjap.40.L1190

Kak AC, Slaney M, IEEE Engineering in Medicine and Biology Society (1988) Principles of computerized tomographic imaging. IEEE Press, New York

Keck B, Hofmann H, Scherl H, Kowarschik M, Hornegger J (2009) GPU-accelerated SART reconstruction using the CUDA programming environment. In: SPIE medical imaging. International Society for Optics and Photonics, pp 72582B–72582B-72589

Konomi M, Fujimoto K, Toda T, Osumi M (2003) Characterization and behaviour of alpha-glucan synthase in *schizosaccharomyces pombe* as revealed by electron microscopy. Yeast 20(5):427–438. doi:10.1002/Yea.974

Lampert F (1971) Coiled supercoiled DNA in critical point dried and thin sectioned human chromosome fibres. Nat New Biol 234(49):187–188

Larabell CA, Le Gros MA (2004) X-ray tomography generates 3-D reconstructions of the yeast, *Saccharomyces cerevisiae*, at 60-nm resolution. Mol Biol Cell 15(3):957–962. doi:10.1091/mbc.E03-07-0522

Le Gros MA, McDermott G, Larabell CA (2005) X-ray tomography of whole cells. Curr Opin Struct Biol 15(5):593–600. doi:10.1016/j.sbi.2006.08.008

Le Gros M, McDermott G, Uchida M, Knoechel C, Larabell C (2009) High-aperture cryogenic light microscopy. J Microsc 235(1):1–8

Leunissen JLM, Yi H (2009) Self-pressurized rapid freezing (SPRF): a novel cryofixation method for specimen preparation in electron microscopy. J Microsc 235(1):25–35

Liang Z, Guan Y, Liu G, Bian R, Zhang X, Xiong Y, Tian Y (2013) Reconstruction of limited-angle and few-view nano-CT image via total variation iterative reconstruction. In: SPIE Optical Engineering + Applications, International Society for Optics and Photonics, pp 885113–885113–885117

McDermott G, Fox DM, Epperly L, Wetzler M, Barron AE, Gros MA L, Larabell CA (2012) Visualizing and quantifying cell phenotype using soft X-ray tomography. Bioessays 34(4):320–327. doi:10.1002/bies.201100125

McDonald K (2007) Cryopreparation methods for electron microscopy of selected model systems. Methods Cell Biol 79:23–56. doi:10.1016/S0091-679x(06)79002-1

Momose A (2005) Recent advances in X-ray phase imaging. Jpn J Appl Phys 44 (Part 1, 9 A):6355–6367. doi:10.1143/Jjap.44.6355

Momose A, Takeda T, Itai Y, Hirano K (1996) Phase-contrast X-ray computed tomography for observing biological soft tissues. Nat Med 2(4):473–475

Mueller K, Yagel R, Wheller JJ (1999) Anti-aliased three-dimensional cone-beam reconstruction of low-contrast objects with algebraic methods. IEEE Tran Med Imaging 18(6):519–537

Muller WG, Heymann JB, Nagashima K, Guttmann P, Werner S, Rehbein S, Schneider G, McNally JG (2012) Towards an atlas of mammalian cell ultrastructure by cryo soft X-ray tomography. J Struct Biol 177(2):179–192. doi:10.1016/j.jsb.2011.11.025

Mulvihill DP, Pollard PJ, Win TZ, Hyams JS (2001) Myosin V-mediated vacuole distribution and fusion in fission yeast. Curr Biol 11(14):1124–1127. doi:10.1016/S0960-9822(01)00322-0

Nett BE, Tang J, Chen GH (2010) GPU implementation of prior image constrained compressed sensing (PICCS). Medical imaging 2010: physics of medical imaging 7622. doi:10.1117/12.844578

Neumann FR, Nurse P (2007) Nuclear size control in fission yeast. J Cell Biol 179(4):593–600. doi:10.1083/jcb.200708054

Pan Y, Whitaker R, Cheryauka A, Ferguson D (2009) Feasibility of GPU-assisted iterative image reconstruction for mobile C-arm CT. In: SPIE medical imaging. International Society for Optics and Photonics, pp 72585J–72585J-72589

Parkinson DY, McDermott G, Etkin LD, Gros MA L, Larabell CA (2008) Quantitative 3-D imaging of eukaryotic cells using soft X-ray tomography. J Struct Biol 162(3):380–386. doi:10.1016/j.jsb.2008.02.003

Parkinson DY, Knoechel C, Yang C, Larabell CA, Le Gros MA (2012) Automatic alignment and reconstruction of images for soft X-ray tomography. J Struct Biol 177(2):259–266. doi:10.1016/j.jsb.2011.11.027

Pfeiffer F, Bunk O, David C, Bech M, Duc G L, Bravin A, Cloetens P (2007) High-resolution brain tumor visualization using three-dimensional X-ray phase contrast tomography. Phys Med Biol 52(23):6923–6930. doi:10.1088/0031-9155/52/23/010

Rafelski SM, Marshall WF (2008) Building the cell: design principles of cellular architecture. Nat Rev Mol Cell Biol 9 (8):593–602. doi:10.1038/nrm2460

Raparia D, Alessi J, Kponou A (1998) The algebraic reconstruction technique (ART). Proceedings of the 1997 Particle Accelerator Conference Vols 1–3:2023–2025

Sajiki K, Hatanaka M, Nakamura T, Takeda K, Shimanuki M, Yoshida T, Hanyu Y, Hayashi T, Nakaseko Y, Yanagida M (2009) Genetic control of cellular quiescence in S-pombe. J Cell Sci 122(9):1418–1429. doi:10.1242/Jcs.046466

Scherfeld D, Schneider G, Guttmann P, Osborn M (1998) Visualization of cytoskeletal elements in the transmission X-ray microscope. J Struct Biol 123(1):72–82. doi:10.1006/jsbi.1998.4017

Schertel A, Snaidero N, Han HM, Ruhwedel T, Laue M, Grabenbauer M, Mobius W (2013) Cryo FIB-SEM: volume imaging of cellular ultrastructure in native frozen specimens. J Struct Biol 184(2):355–360. doi:10.1016/j.jsb.2013.09.024

Schneider G, Guttmann P, Heim S, Rehbein S, Mueller F, Nagashima K, Heymann JB, Muller WG, McNally JG (2010) Three-dimensional cellular ultrastructure resolved by X-ray microscopy. Nat Methods 7(12):985–987. doi:10.1038/nmeth.1533

Sidky EY, Pan XC (2008) Image reconstruction in circular cone-beam computed tomography by constrained, total-variation minimization. Phys Med Biol 53(17):4777–4807. doi:10.1088/0031-9155/53/17/021

Sidky EY, C-MKa o, XcP n (2006) Accurate image reconstruction from few-views and limited-angle data in divergent-beam CT. J Xray Sci Technol

Smith EA, Cinquin BP, Do M, McDermott G, Gros MA L, Larabell CA (2013) Correlative cryogenic tomography of cells using light and soft X-rays. Ultramicroscopy 143:33–40. doi:10.1016/j.ultramic.2013.10.013

Takagi T, Ishijima SA, Ochi H, Osumi M (2003) Ultrastructure and behavior of actin cytoskeleton during cell wall formation in the fission yeast *schizosaccharomyces pombe*. J Electron Microsc 52(2):161–174. doi:10.1093/jmicro/52.2.161

Tian YC, Li WJ, Chen J, Liu LH, Liu G, Tkachuk A, Tian JP, Xiong Y, Gelb J, Hsu G, Yun WB (2008) High resolution hard x-ray microscope on a second generation synchrotron source. Rev Sci Instrum 79(10). doi:10.1063/1.3002484

Tian Z, Jia X, Yuan KH, Pan TS, Jiang SB (2011) Low-dose CT reconstruction via edge-preserving total variation regularization. Phys Med Biol 56(18):5949–5967. doi:10.1088/0031-9155/56/18/011

Uchida M, McDermott G, Wetzler M, Gros MA L, Myllys M, Knoechel C, Barron AE, Larabell CA (2009) Soft X-ray tomography of phenotypic switching and the cellular response to antifungal peptoids in Candida albicans. Proc Natl Acad Sci U S A 106(46):19375–19380. doi:10.1073/pnas.0906145106

Uchida M, Sun Y, McDermott G, Knoechel C, Gros MA L, Parkinson D, Drubin DG, Larabell CA (2011) Quantitative analysis of yeast internal architecture using soft X-ray tomography. Yeast 28(3):227–236. doi:10.1002/yea.1834

Vila-Comamala J, Pan Y, Lombardo JJ, Harris WM, Chiu WK, David C, Wang Y (2012) Zone-doubled fresnel zone plates for high-resolution hard X-ray full-field transmission microscopy. J Synchrotron Radiat 19 (5):705–709. doi:10.1107/S0909049512029640

Wang G, Jiang M (2004) Ordered-subset simultaneous algebraic reconstruction techniques (OS-SART). J Xray Sci Technol 12(3):169–177

Weiss D, Schneider G, Niemann B, Guttmann P, Rudolph D, Schmahl G (2000) Computed tomography of cryogenic biological specimens based on X-ray microscopic images. Ultramicroscopy 84(3):185–197

Williams IM, Siu KK, Gan R, He X, Hart SA, Styles CB, Lewis RA (2008) Towards the clinical application of X-ray phase contrast imaging. Eur J Radiol 68 (3 Suppl):73–77. doi:10.1016/j.ejrad.2008.04.042

Yang Y, Li W, Liu G, Zhang X, Chen J, Wu W, Guan Y, Xiong Y, Tian Y, Wu Z (2010) 3D visualization of subcellular structures of *schizosaccharomyces pombe* by hard X-ray tomography. J Microsc 240(1):14–20. doi:10.1111/j.1365–2818.2010.03379.x

Zeng GL (2010) Medical image reconstruction: a conceptual tutorial. Springer, New York

Zeng XH, Duewer F, Feser M, Huang C, Lyon A, Tkachuk A, Yun WB (2008) Ellipsoidal and parabolic glass capillaries as condensers for x-ray microscopes. Appl Opt 47(13):2376–2381. doi:10.1364/Ao.47.002376

Zhang JC, Cai XQ, Zhang Y, Li XM, Li WX, Tian YC, Li AG, Yu XH, Fan CH, Huang Q (2013) Imaging cellular uptake and intracellular distribution of TiO_2 nanoparticles. Anal Methods 5(23):6611–6616. doi:10.1039/C3ay41121d

Zheng T, Li WJ, Guan Y, Song XX, Xiong Y, Liu G, Tian YC (2012) Quantitative 3D imaging of yeast by hard X-ray tomography. Microsc Res Tech 75(5):662–666. doi:10.1002/Jemt.21108